Fermi National Accelerator Laboratory

Deflecting Modes of the Side-Coupled Cavity Structure

Shigemi Inagaki
Fermi National Accelerator Laboratory
P.O. Box 500
Batavia, Illinois 60510

November 1990

Deflecting Modes of the Side-Coupled Cavity Structure

Shigemi INAGAKI*

Fermilab, Batavia, IL 60510, USA

Abstract

The deflecting modes of the 805 MHz side-coupled cavity structure with the relativistic factor 0.566 are studied. Our main concern is the dispersion properties among different configurations of side-coupling cells and their interpretations. It is shown that the ninety degree side-coupling cell configuration, so to speak, the Mickey Mouse configuration has a merit in reducing the HEM_1 passband. Another concern is the magnitude of the transverse coupling impedance around the synchronization condition. It is shown that the existence of the coupling cell introduces the nonuniformity of the deflecting mode and gives different impedance relative to the beam axis and that the coupling impedance at $\pi/10$ exceeds 50 MΩ/m if the quality value of the mode is around 12000.

1. Introduction

The so-called $\pi/2$ mode standing wave structures are frequently used for high energy proton linear accelerators and electron synchrotron/storage rings. The extraordinary stability of the resonant field cannot be overvalued.[1],[2] Among them the side-coupled cavity structure (SCC)[3] was adopted for the 800 MeV proton linear accelerator in the Los Alamos Meson Physics Facility (LAMPF) and has been in

---

* present address   National Laboratory for High Energy Physics

1-1 Oho, Tsukuba-shi, Ibaraki-ken, 305, Japan

operation for more than twenty years. The structure has further been adopted in many electron accelerators for various application purposes. As the linac upgrade project, Fermilab is also going to use the structure.

The alternating periodic iris loaded wave guide structure (APS)[4] and the disk-and-washer structure (DAW)[5] are other examples of $\pi/2$ mode standing wave structures. The former found its way for the TRISTAN main ring in National Laboratory for High Energy Physics (KEK). The latter has been under development for the 600 MeV proton linac at the Radiotechnical Institute in the USSR. The structure was also used for the TRISTAN accumulation ring for a while. The extensive studies of deflecting modes in the APS and DAW including the dispersion curve and the coupling impedance as well as the comparison with beam experiments[6],[7] have been made in KEK, since the particle to be accelerated and stored in KEK is electron and positron rather than proton and the deflecting mode could cause severe beam stability problems.

However, as far as the SCC is concerned, much is not studied except the general consideration of transverse modes by Potter[8] and the dispersion measurement for the Los Alamos/NBS racetrack microtron[9]. Therefore, in this occasion to convert a part of the 200 MeV Alvarez linac into a 400 MeV SCC linac, we have studied the dispersion properties and the transverse coupling impedance using a 6-gap aluminum model cavity.

As the Fermilab linac upgrade project to increase the injection energy to the booster from 200 MeV to 400 MeV, the high energy part of the Alvarez cavities will be replaced by the side-coupled cavities. The accelerating frequency is 805 MHz, which is four times that of the existing linac. As the injector for the booster, the required beam current is 50 mA for the pulse length of 100 μs with the repetition rate 15 Hz. One of the distinguished features of the new linac is the average axial field around 8 MV/m, which requires maximum surface field of 37.1 MV/m as compared to the Kilpatrick limit of 26 MV/m. The SCC linac consists of seven modules, each of which is excited by a same klystron about 9 MW. The module consists of four sections mutually excited through bridge couplers. And one section has sixteen gaps, with an identical cell-geometry of the average energy. Therefore we assume 28 different cavities, each of

which has a exact periodicity except both end cells.

2. Measurement of Dispersion Curve

For the study of the deflecting modes we used a six-gap aluminum cavity. As is shown schematically in Fig. 1, the whole structure consists of 7 accelerating cell units (Fig. 2a) and 5 coupling cell units (Fig. 2b). Both ends of five accelerating cell units (normal cell unit) and one end of two remaining units (end-cell units) are machined into half accelerating cells. Coupling slots are cut on the normal cell units. A coupling cell unit is connected to a normal cell unit by two tightening belts to have rf coupling between the neighboring cells as shown in Fig. 2c. The stack of the whole units makes a cavity with six accelerating and five coupling cells. Among them only one end-cell has a tuning mechanism, i.e. the protrusion of the nose cone is variable. We denote the cell as No. 1, and affix the order sequentially. Fig. 3 shows the dimension of the half accelerating cell that corresponds to the relativistic factor 0.566 or 200 MeV.

To measure the azimuthal symmetry, holes 1.5625 mm in diameter are drilled on the side wall of each accelerating cell in every 15 degrees. They are offset by 12.7 mm from the middle plane of the cell. Twelve holes of the same size are drilled in every 30 degrees parallel to the axis on both end cells. Probes made of semirigid coaxial cable (UT-141) are inserted through these holes to pick up the electric or magnetic field. We tuned the 6-gap cavity so that the field distribution of the accelerating mode becomes as flat as possible (Fig. 4). Thereafter we measured the resonant frequency of each cell by using shortening rods for accelerating cells and shortening plungers for coupling cells. The results are shown in Table 1. The frequency of No. 1 cell was about 0.3 % lower than the average frequency of the other five cells, meanwhile the difference between the five cells was less than 0.035 %.

For the given dimension, we computed parasitic modes by the aid of URMEL[13] for a single cell. Some of lower resonances are shown in Table 2. The modes are assigned according to the analogous field of a cylindrical cavity, but * indicates that the

field distribution drawn by URMEL differs so much from that of the cylindrical cavity. The modes with a half-period variation of E or H in neighbouring accelerating cells are denoted as having $\pi/2$ phase shift per cell.

Referring to the calculation, and the azimuthal, axial and transverse variation of the field we assigned 11 modes among 27 resonances below 3 GHz for a single cell configuration. Then we increased to two cells, three cells, four cells and then six cells. The phase difference between two points is known easily by the aid of a network analyzer. We feed rf signal to a fixed reference position and measure S_{21} at the two points using same cables and probes. The phase difference between the pickup signals gives the phase difference between the two points. Table 3 shows the case of HEM_1 passband of the staggered configuration (described below). In this case the electrically coupling feeder is connected to the end plate, and the signal is picked up from the side wall at the same azimuth of each cell. ϕ denotes the phase relative to the feeder. $\Delta\phi$ is the phase difference between the neighboring cells. It is either 0 or π, so that the mode with resonant frequency 1.447 GHz can be assigned as $1/10\ \pi$ mode and that with 1.366 GHz can be assigned $1/2\ \pi$ mode.

In the case of TM_{11}-like modes, there are two polarizations relative to the coupling cell as shown in Fig. 5. For convenience sake, we denote the mode with the central part of the magnetic field directed to the coupling cell by $H_\perp$ and that with the central part of the magnetic field perpendicular to the direction of the coupling cell by $H_{//}$. It can be expected that the coupling between the accelerating and coupling cell for $H_\perp$ is weaker than that for $H_{//}$. As will be shown in the dispersion curve $H_{//}$ has a wide passband, but the resonances for $H_\perp$ are so weakly excited that drawing of the dispersion curve is almost impossible. In the case of TE_{21}-like modes, $E_\perp$ denotes the mode where the electric field terminates to the coupling cell, and the other distribution is denoted by $E_{//}$ (Fig. 6).

We measured the dispersion for three different configurations of side-coupling cells. The first is the staggered configuration where the neighboring coupling cells are located to opposite side relative to the beam axis (Fig. 7a). The second is the aligned

configuration where all the coupling cells are aligned to one azimuthal position (Fig. 7b). The third is the Mickey Mouse configuration where the neighboring coupling cells are located by 90° relative to beam axis (Fig. 7c). We did not measure the spiral configuration like Fig. 7d, as it looks unpractical or too complicated to install on a support guarder. Figs. 8a, 8b and 8c show the dispersion curve corresponding to the configurations of Fig. 7a, 7b and 7c, respectively. The field distribution of many of the modes are so distorted from that of a cylindrical cavity that the passbands are preferably to be denoted as HEM ones. Therefore, the notation in Fig. 8 is attached to a single resonance on the edge of the passband and is intended to indicate the corresponding cylindrical cavity modes.

For all three configurations, the TM_0 accelerating passband is almost unchanged. The bandwidth is 43.443 MHz, 41.348 MHz and 43.782 MHz, respectively. In the meantime, HEM_1 passbands are very different from each other. For the staggered configuration HEM_1 passband has two branches and it looks as if the two branches are made confluent at 0 phase shift. If we extend the concept of the confluence at π mode there should be two different boundary conditions for a single cell, and with the same resonant frequency at 0 phase shift. Fig. 12 suggests that the lower HEM_1-$\pi/2$ mode is derived from TM_{111} of a cylindrical cavity. The azimuthal dependence of the 1.674 GHz mode is more or less ambiguous. It rather looks like $l = 0$, but Fig. 13 suggests that it resembles something like TE_{111} mode at end cells. Therefore the two branches of the staggered configuration look to be related with the confluence of TM_{11} and TE_{11} passbands. However, the frequency of TE_{111} is never higher than that of TM_{111} mode for a fixed D/L ratio of the cylindrical cavity. For the case of the aligned configuration, the HEM_1 passband is much wider than that of the staggered configuration. It ranges from 1.404 to 1.772 GHz and consists of three branches. On the other hand, in the case of the Mickey Mouse configuration, the HEM_1 modes are very weakly excited. In other words, two different orientations of the coupling cells isolate the two polarizations and confine the excitation of deflecting modes only into two accelerating and one coupling cells and suppress the propagation. The HEM_1 passband looks to be separated into three narrow

bands 1.400 ~ 1.410 GHz, 1.477 ~ 1.480 GHz and 1.630 ~ 1.638 GHz. The bandwidth is almost 7 % of the staggered configuration. Thus Mickey Mouse configuration has a merit over two others from the dispersion point of view.

3. Transverse Coupling Impedance

We define the transverse coupling impedance of a cavity structure by the following formula.

$$Z_\perp(\omega) = \frac{Q_a \left| v_{//} \right|^2/\epsilon\omega_a k}{1 + jQ_a(\omega/\omega_a - \omega_a/\omega)} \equiv \frac{R_\perp \omega_a/\omega}{1 + jQ_a(\omega/\omega_a - \omega_a/\omega)} \quad , \quad (1)$$

where Q_a and ω_a represent the quality value and the angular frequency of a resonant mode a, $k = \omega/v$ and

$$v_{//}^* = \int grad\ E_{az}\ e^{-jkz}\ dz \quad . \tag{2}$$

$v_{//}$ is related to the transverse field by

$$\frac{v_{//}}{R} = v_\perp \quad , \tag{3}$$

where

$$v_\perp = j\int E_{ay}\ e^{jkz}\ dz - \frac{k_a}{k}\int H_{ax}\ e^{jkz}\ dz \quad . \tag{4}$$

Equation (1) is derived from the usual definition of the transverse coupling impedance

$$Z_\perp = \lim_{\Delta \to 0}\frac{\int [\ E + v\ x\ B]_\perp e^{jkz}\ dz}{I\Delta} \quad , \tag{5}$$

after some manipulation based upon the normal modes expansion[10],[11].

In order to pick up the field component, we use the perturbation due to an ellipsoidal object formulated by Maier and Slater[12]. In the case of a needle, the frequency shift Δf is given by

$$\frac{\Delta f}{f_0} = \frac{3}{2} \cdot \frac{4\pi}{3} a^3 (-E_{0//}^2\ F_1\ (\eta) - E_{0\perp}^2 F_6(\eta)$$

$$+ \frac{1}{2} H_{0//}^2\ F_3\ (\eta) + \frac{1}{2} H_{0\perp}^2 F_4\ (\eta)) \quad , \tag{6}$$

and in the case of a disk, it is given by

$$\frac{\Delta f}{f_0} = \frac{3}{2} \cdot \frac{4\pi}{3} a^3 \left(-E_{0\!/\!/}^2 F_5 (\eta) - E_{0\perp}^2 F_6 (\eta) \right.$$

$$\left. + \frac{1}{2} H_{0\perp}^2 F_7 (\eta) + \frac{1}{2} H_{0\!/\!/}^2 F_8 (\eta) \right) \quad , \tag{7}$$

where a is the semi-major axis and η is the ratio of the minor axis to major axis. $\perp$ and $/\!/$ denote that the field is vertical and parallel to the major axis, respectively. The suffix 0 denotes the unperturbed quantity. The detailed expressions of $F_i(\eta)$ should be referred to Ref. (12). They reflect a physical meaning that a needle is most sensitive to the electric field parallel to the major axis, and that a disk is sensitive to the electric field parallel to the major axis and to the magnetic field perpendicular to the major axis.

4. Measurement of the Coupling Impedance

The needles or disks used to measure the transverse coupling impedance were made by a numerically controlled lathing machine. The tolerance of the machining is $\pm$ 0.198 mm. As we have not calibrated them in a standard field and we measured the frequency shift manually, which inevitably accompanied the drift caused by many reasons, we limit ourselves to a qualitative discussion here. We report only the staggered coupling cell configuration, which will be adopted in Fermilab upgrade linac. We measured the transverse coupling impedance near the synchronization condition, i.e., the crosspoint of dispersion curve with $f = 2f_0/\pi \cdot \phi$ line.

Fig. 9 shows the perturbed frequency of HEM_1-0 mode due to a needle with the semi-major axis 6.35 mm and the minor axis 1.59 mm. The perturber is displaced 10 mm above or below the center axis. (We have three coupling cells on one side and two coupling cells on the other side. We denote here "above" for three cell side and "below" for the two cell side.) The data shows that the field above the axis is magnetic and that below the axis is electric in No. 1, 3 and 6 cells and is reversed in No. 2, 4 and 5 cells. This fact results in different transverse coupling impedance, or the different effect to the beam depending upon the path above or below the axis. The measured values are as follows:

$$R/Q = 165 \ \Omega/m \qquad \text{above the axis}$$

$$= 550 \ \Omega/m \qquad \text{below the axis.}$$

Using an ellipsoidal disk with 6.35 mm in major axis and 1.59 mm in minor axis, we measured the magnetic field on the axis denoted by dotted line in Fig. 9b. This gives

$$R/Q = 660 \ \Omega/m,$$

which should coincide with the value calculated by a needle measurement if the field is not asymmetric.

For the HEM_1 - $\pi/10$ mode (1.447 GHz), the needle measurement shows the field above the axis is different from that below the axis (Fig. 10) as the case of HEM_1-0 mode. However, the numerical value of the transverse coupling impedance is not so different.

$$R/Q = 420 \ \Omega/m \qquad \text{above the axis}$$

$$= 423 \ \Omega/m \qquad \text{below the axis.}$$

Meanwhile, the disk-perturbed data gives

$$R/Q = 366 \ \Omega/m \qquad \text{on the axis.}$$

For the HEM_1-$\pi/10$ mode (1.525 GHz), the longitudinal electric field below the axis is stronger than that above the axis in No. 2 and 5 cells (Fig. 11a). The value of the transverse coupling impedance is

$$R/Q = 3.84 \ k\Omega/m \qquad \text{above the axis}$$

$$= 4.99 \ k\Omega/m \qquad \text{below the axis,}$$

by the needle measurement, and

$$R/Q = 358 \ \Omega/m$$

by the disk measurement.

The impedance of HEM_1-$\pi/2$ mode (1.366 GHz, Fig. 12) is measured by the disk to give

$$R/Q = 954 \ \Omega/m \qquad \text{on the axis}$$

and that of HEM_1-$\pi/2$ mode (1.674 GHz, Fig. 13) is

$$R/Q = 304 \ \Omega/m \qquad \text{on the axis.}$$

5. Conclusion

The deflecting modes of the SCC were studied by aluminum models, which corresponds to the energy of 200 MeV for Fermilab linac upgrade.

The dispersion properties of the three different coupling-cell configuration were measured. The HEM_1 passband has two polarizations $H_\perp$ and $H_{//}$ relative to the coupling cell, and it couples weaker to $H_\perp$ than $H_{//}$. Therefore, if we change the direction of the coupling cells by 90° alternately, we can reduce the HEM_1 coupling throughout the cavity and also make the passband narrow.

For the staggered configuration, the HEM_1 passband is made confluent at 0-phase shift, and for the aligned configuration it is made confluent at 0 and $\pi/2$ phase shift.

The measurement of the transverse coupling impedance near the synchronization condition shows that the value above and below the axis is very different for some phase points. This could make the real assessment of the deflection complicate. The resonances at $\pi/10$ (1.525 GHz) has an order of magnitude higher value than that of $\pi/10$ (1.447 GHz), but this would not be fatal for a proton accelerator. However, the real effect of the upper passband must be measured around $\pi/12$ and $\pi/8$ for the actual cavity.

Acknowledgement

References

(1) T. Nishikawa, S. Giordano and D. Carter, "Dispersion Relation and Frequency Characteristics of Alternating Periodic Structure for Linear Accelerators", Rev. Sci. Instrum. 37 (1966) 652.

(2) D. E. Nagle, E. A. Knapp and B. C. Knapp, "Coupled Resonator Model for Standing Wave Accelerator Tanks", Rev. Sci. Instrum. 38 (1067) 1583.

(3) E. A. Knapp, B. C. Knapp and J. M. Potter, "Standing Wave High Energy Linear Accelerator Structures", Rev. Sci. Instrum. 39 (1968) 979.

(4) S. Giordano, "Some New Radio Frequency Accelerating Structures", IEEE Trans. Nucl. Sci. NS-12 (1965) 213.

(5) V.G. Andreev, V. M. Belugin, V. G. Kulman, E. A. Mirochnik and B. M. Pirozhenko, "Study of High-Energy Proton linac Structures", Proc. 1972 Proton Linac Conf. LA-5115 (1972), p.114.

(6) T. Higo, Y. Yamazaki, T. Ieiri, K. Nakajima, T. Kageyama, M. Akemoto, Y. Morozumi and K. Takata, "Quantitative Test of Theory for Transverse Coupled Bunch Instability due to Multi-Cell Cavity in Electron Storage Ring", to be published.

(7) S.Inagaki, "Disk-and-Washer Cavities for an Accelerator", Nucl. Instrum. Methods Phys. Res. A251 (1986) 417.

(8) J. M. Potter, "Transverse Modes in a Resonantly Coupled Accelerator", Proc. 1966 Linac Conf. Los Alamos LA-3609 (1966) p.109.

(9) R. K. Cooper, Y. Iwashita, J. M. Potter, S. O. Schriber, D. A. Swenson, J. M. Watson, L. C. Wilkerson and L. M. Young, "Radio-Frequency Structure Development for the Los Alamos/NBS Racetrack Microtron", LA-UR-83-95 (1983).

(10) Y. Yamazaki, K. Takata and S. Tokumoto, "Measurement of the Longitudinal and Transverse Coupling Impedance of the Higher-order Modes of the Re-Entrant Accelerating Cavity", KEK-80-8 (1980).

(11) T. Suzuki, "Comments on Yamazaki's Theorem", KEK informal circulation, 10
      Dec. 1982.

(12) L.C. Maier and J. C. Slater, "Field Strength Measurements in Resonant Cavities",
      Journ. Appl. Phys. 23 (1952) 68.

(13) T. Weiland, "On the Computation of Resonant Modes in Cylindrically Symmetric
      Cavities", Nucl. Instrum. Methods 216 (1983) 329.

Table 1   Acceleration frequency of individual cell

Cell Number	Frequency of Individual Cell (MHz)
1	804.4373
2	807.1998
3	806.9123
4	807.2745
5	807.2868
6	806.3623

Table 2   Some fundamental resonances of an accelerating cell

Boundary Condition	Frequency (MHz)	$(R/Q)/(kr_0)^2 l$ (Ω)	Q	R ($M\Omega/m$)	Mode
0-EE	800.85				TM_{010}
1-EE	1484.92	16.763	29391	15.332	TM_{110}
0-EE	1806.08				TM_{020}
2-EE	1939.58	0.360			TM_{210}
1-ME	1972.17	1.803	25893	1.930	TE_{111}
2-ME	2155.87	0.116			TE_{211}
1-ME	2499.03	0.877	33488	1.538	TM_{111}*
1-EE	2523.66	2.245	36505	4.335	TM_{120}
1-ME	2742.47	1.232			*

Table 3   Phase shift between accelerating cells

Frequency (GHz)	Phase (Deg)	Cell						Mode
		1	2	3	4	5	6	
1.3662	ϕ	161	-44.6	170.3	0	164.5	-41.8	$\frac{5}{5}\frac{\pi}{2}$
	$\Delta\phi$	-205.6	214.9	-170.3	164.5	-206.3		
1.3773	ϕ	126.9	-55.4	122.7	159.6	-54.1	115.3	$\frac{4}{5}\frac{\pi}{2}$
	$\Delta\phi$	-182.3	178.1	36.9	-213.7	169.4		
1.3955	ϕ	15.3	-151.3	-155.1	17.2	17.4	-159.7	$\frac{3}{5}\frac{\pi}{2}$
	$\Delta\phi$	-166.6	-3.8	172.3	0.2	-177.1		
1.4188	ϕ	-34.5	154.5	150.6	163.7	-62.3	-37.7	$\frac{2}{5}\frac{\pi}{2}$
	$\Delta\phi$	189	-3.9	13.1	-226	24.6		
1.4473	ϕ	-100.3	-94.6	-100.7	76.1	74.4	80.0	$\frac{1}{5}\frac{\pi}{2}$
	$\Delta\phi$	5.7	-6.1	176.8	-1.7	5.6		
1.4588	ϕ	-126.5	-120.8	-127.9	126.0	-131.6	-124.1	0
	$\Delta\phi$	5.7	-7.1	1.9	-5.6	7.5		
1.525	ϕ	-10.9	-2.3	-13.5	0	0	157.0	$\frac{1}{5}\frac{\pi}{2}$
	$\Delta\phi$	8.6	-11.2	13.5	0	157		
1.5596	ϕ	-142.5	-144.7	-144.6	34.0	33.3	-144.7	$\frac{2}{5}\frac{\pi}{2}$
	$\Delta\phi$	-2.2	0.1	178.6	-0.7	-178		
1.596	ϕ	128.8	133.9	-47.0	128.7	128.9	-43.7	$\frac{3}{5}\frac{\pi}{2}$
	$\Delta\phi$	5.9	-180.9	175.7	0.2	-172.6		
1.6336	ϕ	8.4	-167.4	-176.6	9.7	-167.5	10.1	$\frac{4}{5}\frac{\pi}{2}$
	$\Delta\phi$	-175.8	-9.2	186.3	-177.2	177.6		
1.6730 *	ϕ	-145.0	30.3	-132.3	29.3	31.4	35.0	$\frac{5}{5}\frac{\pi}{2}$?
	$\Delta\phi$	175.3	-162.6	161.6	2.1	3.6		
1.6937 *	ϕ	1355	-50.0	124.8	-59.3	127.3	134.8	$\frac{4}{5}\frac{\pi}{2}$
	$\Delta\phi$	-185.5	174.8	-184.1	186.6	7.5		

* looks like 1 = 0
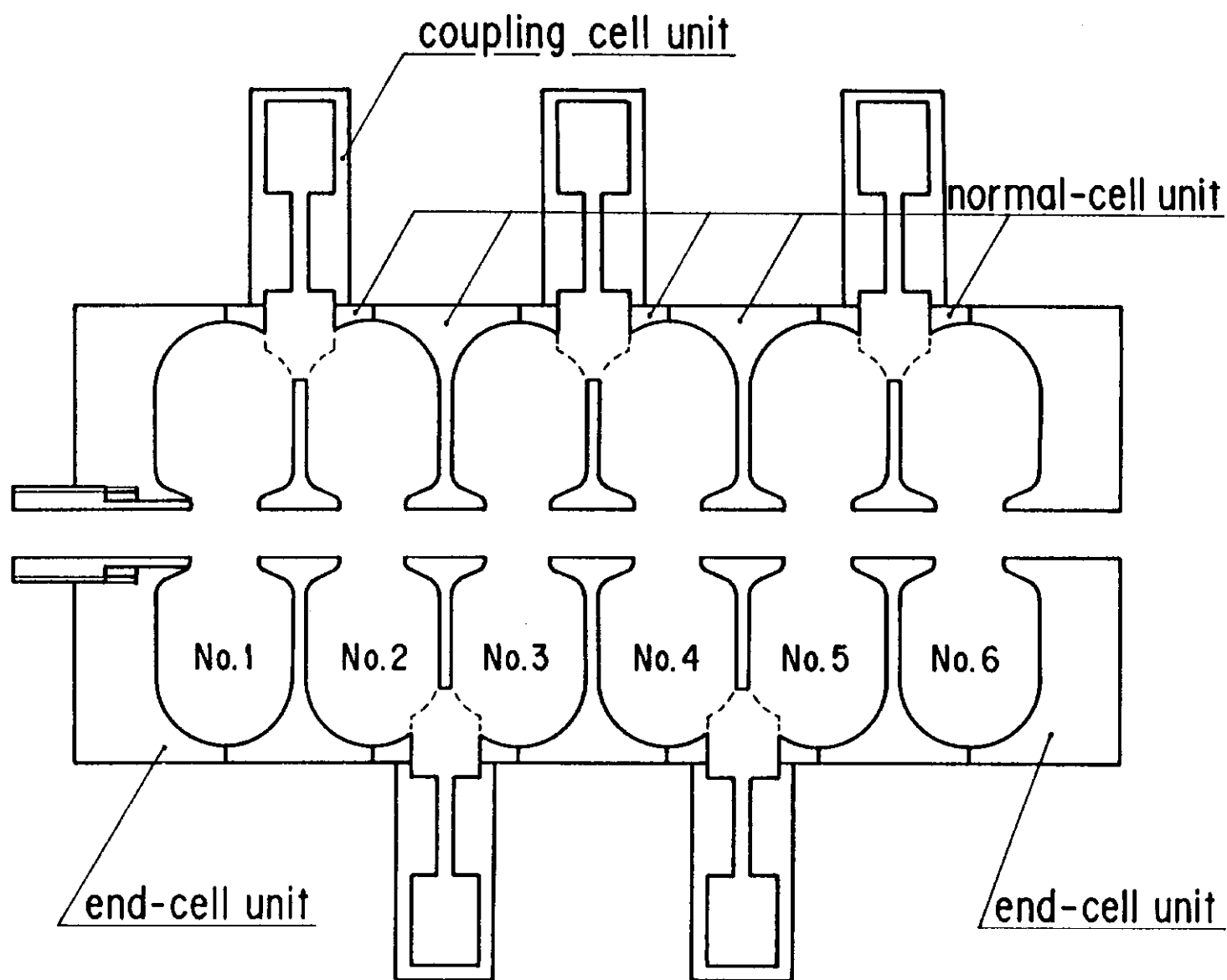
Fig. 1   Six gap aluminum model cavity.
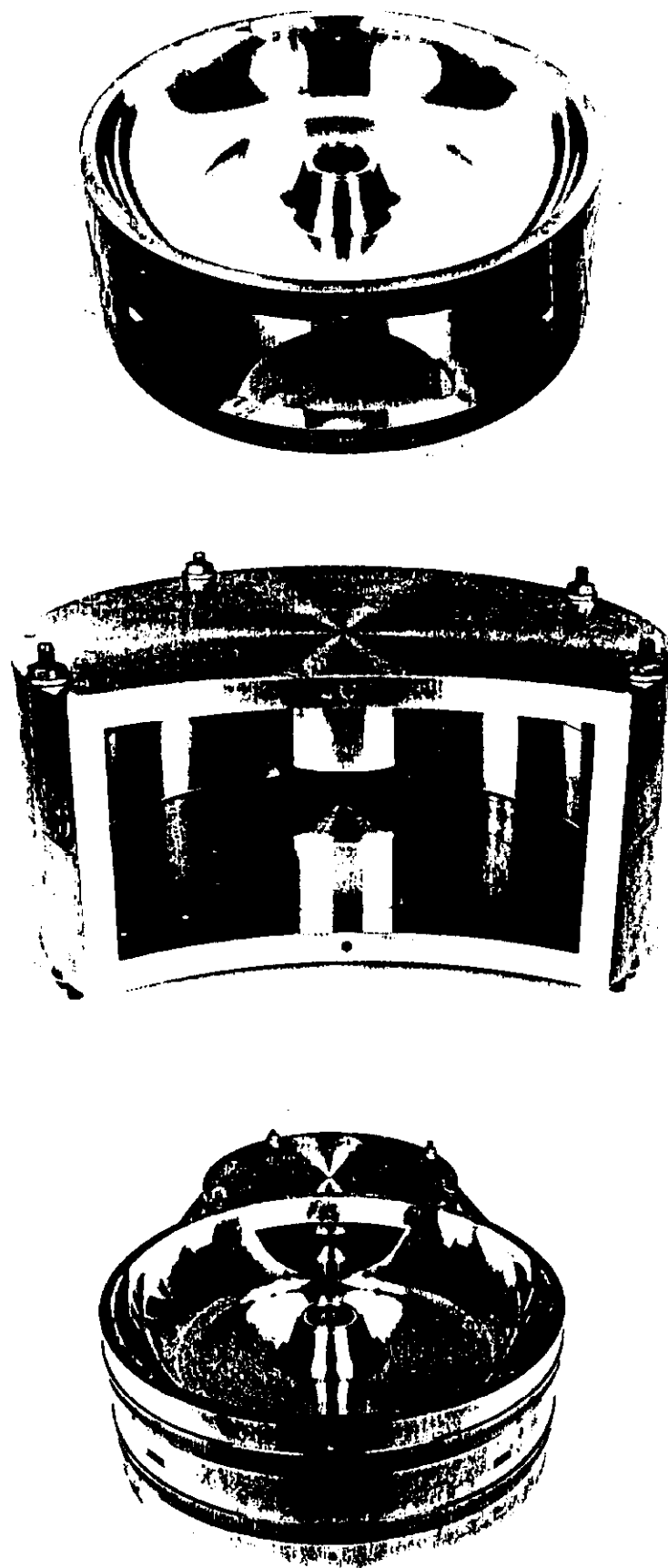
Fig. 2a, b and c   Accelerating, coupling and assembled cell unit (t-b).
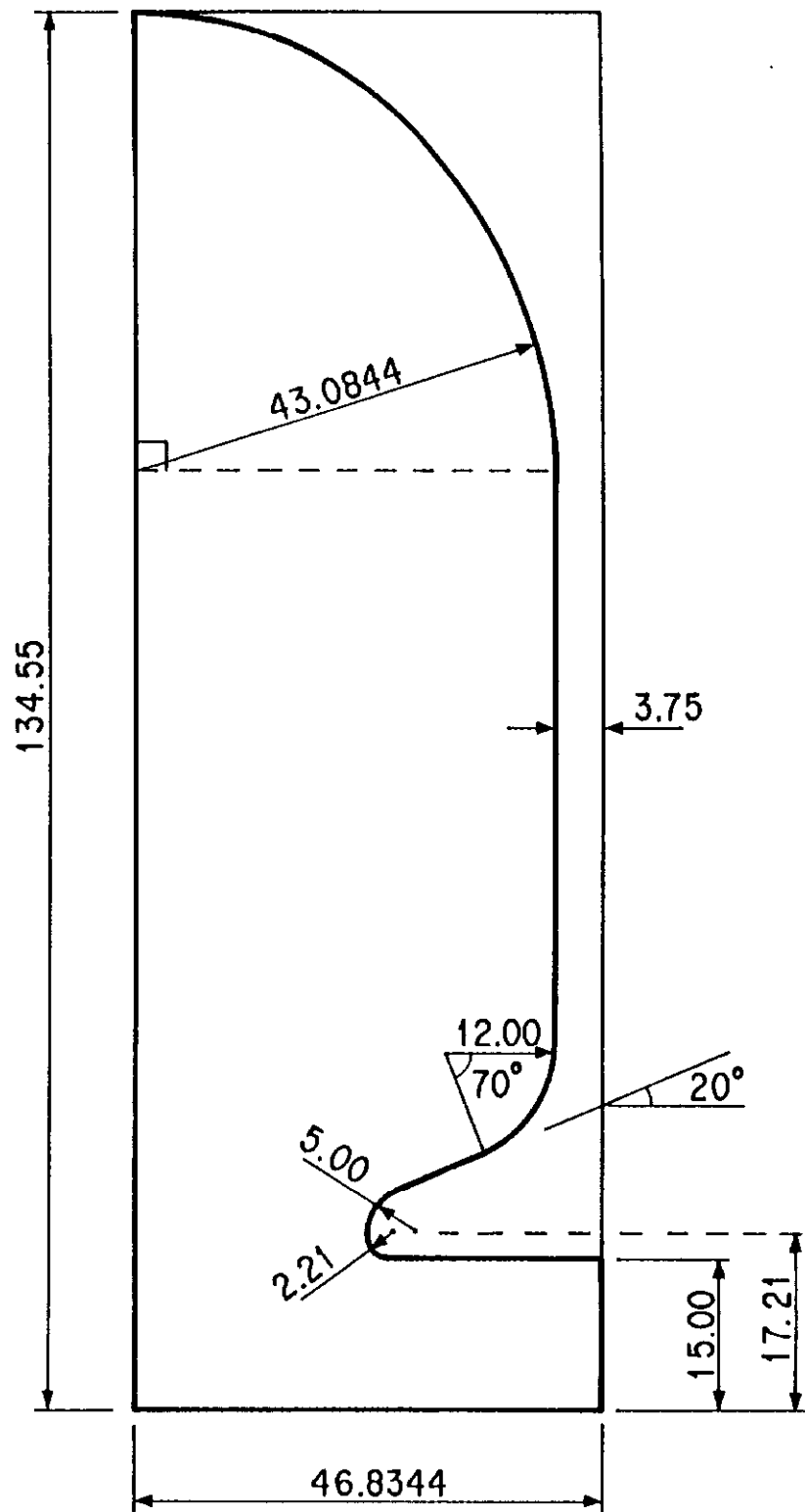
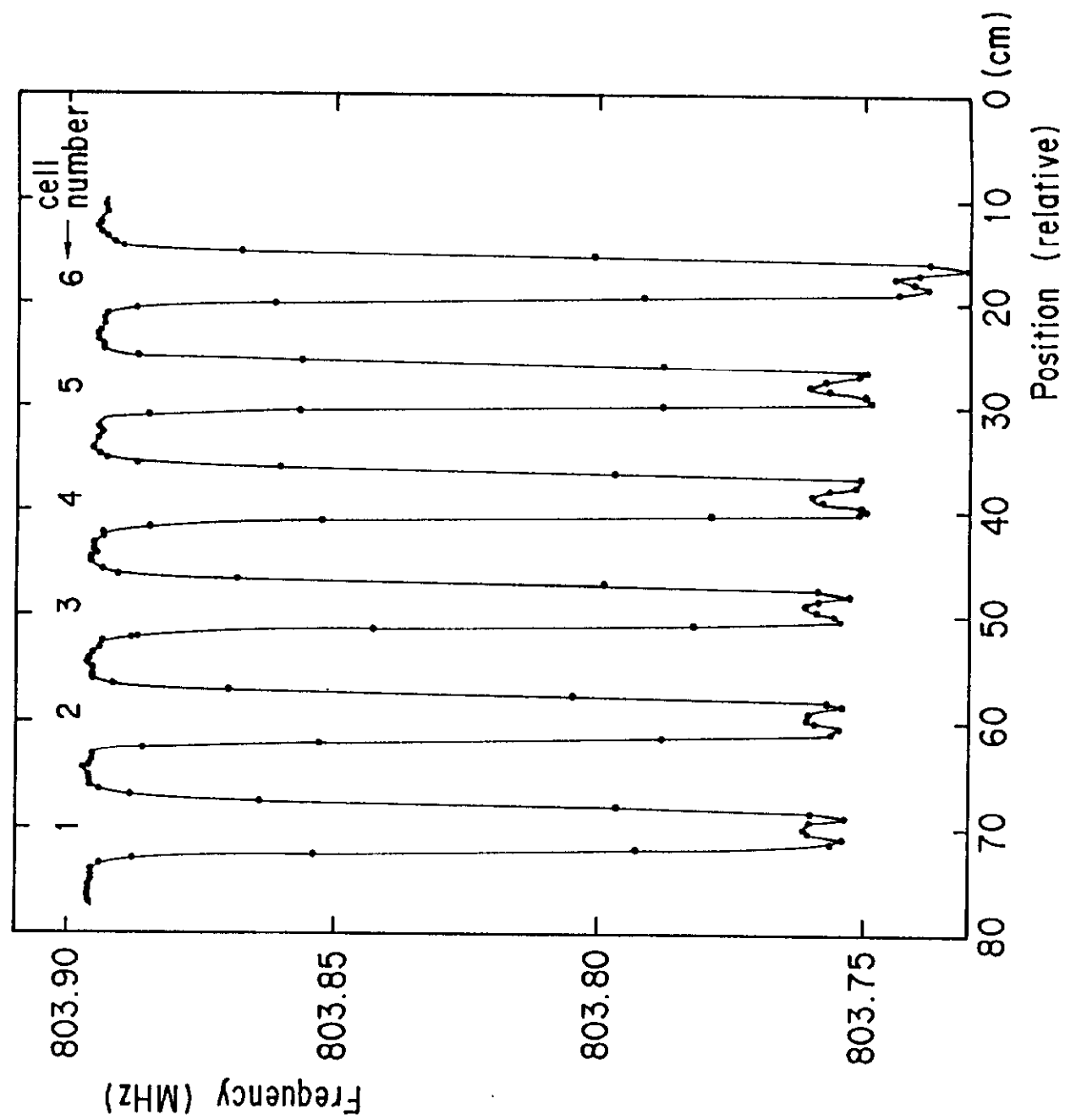Fig. 3   Dimension of the half accelerating cell.

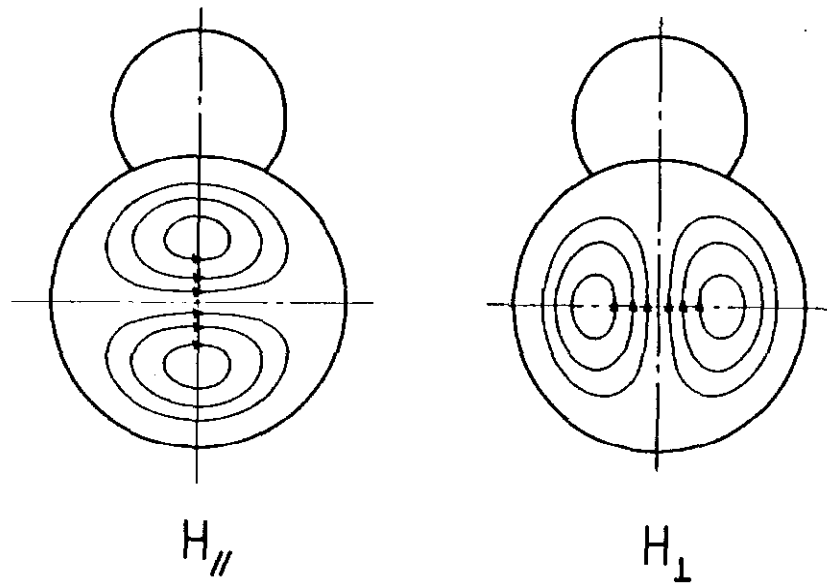Fig. 4   Frequency shift of the accelerating mode due to a metalic sphere.

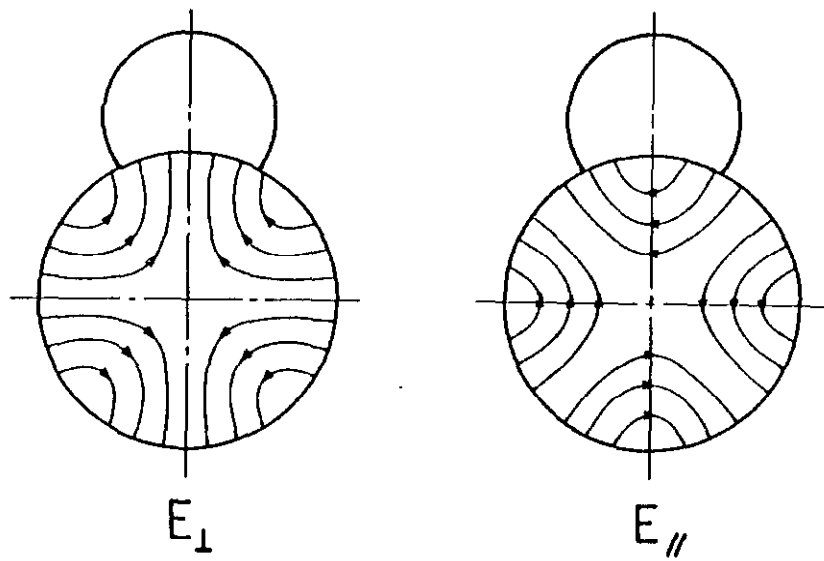Fig. 5   Two polarizations of TM_{11}-like modes.
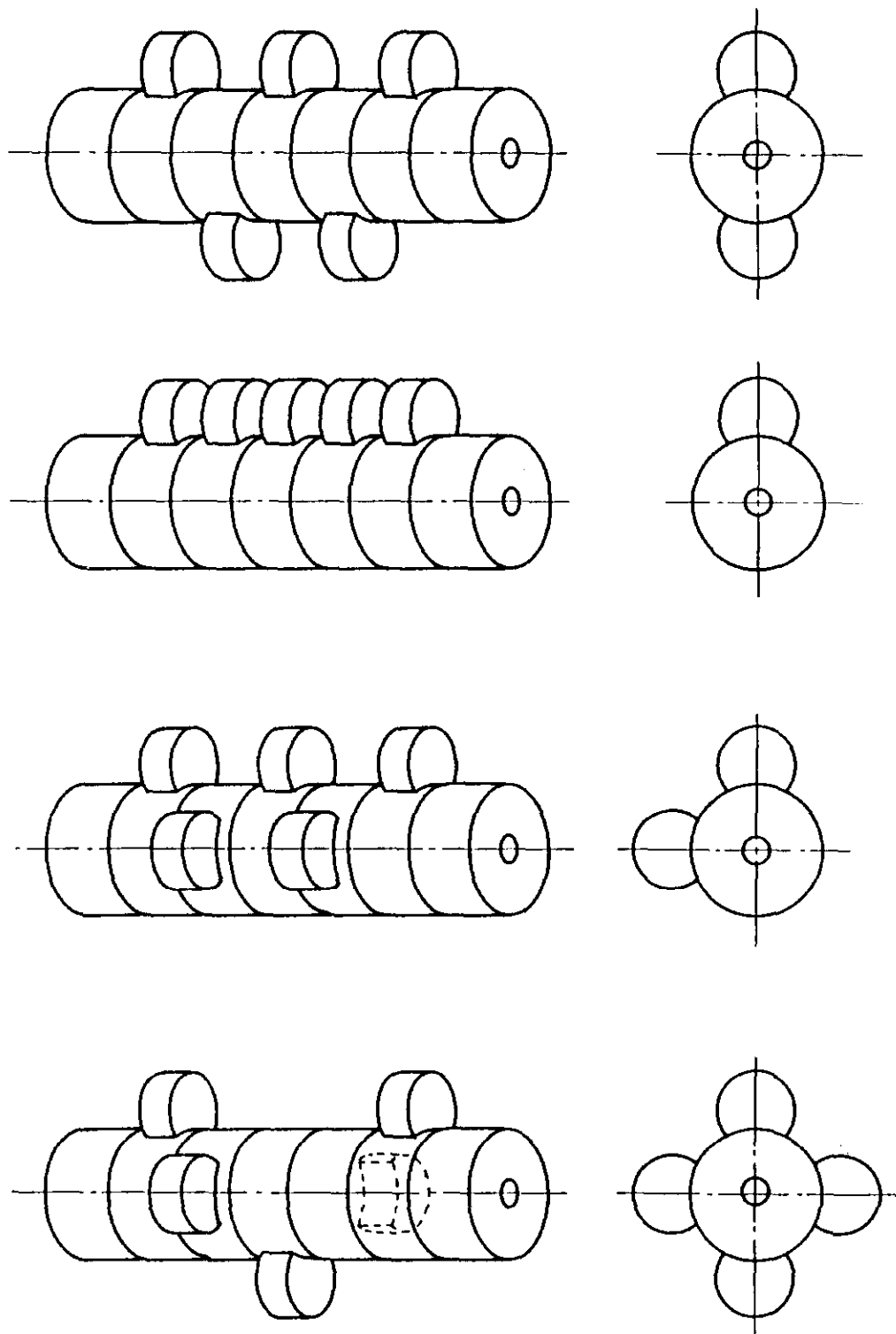

Fig. 6   Two polarizations of TE_{21}-like modes.

Fig. 7a, b, c and d   Staggered, aligned, Micky Mouse and spiral
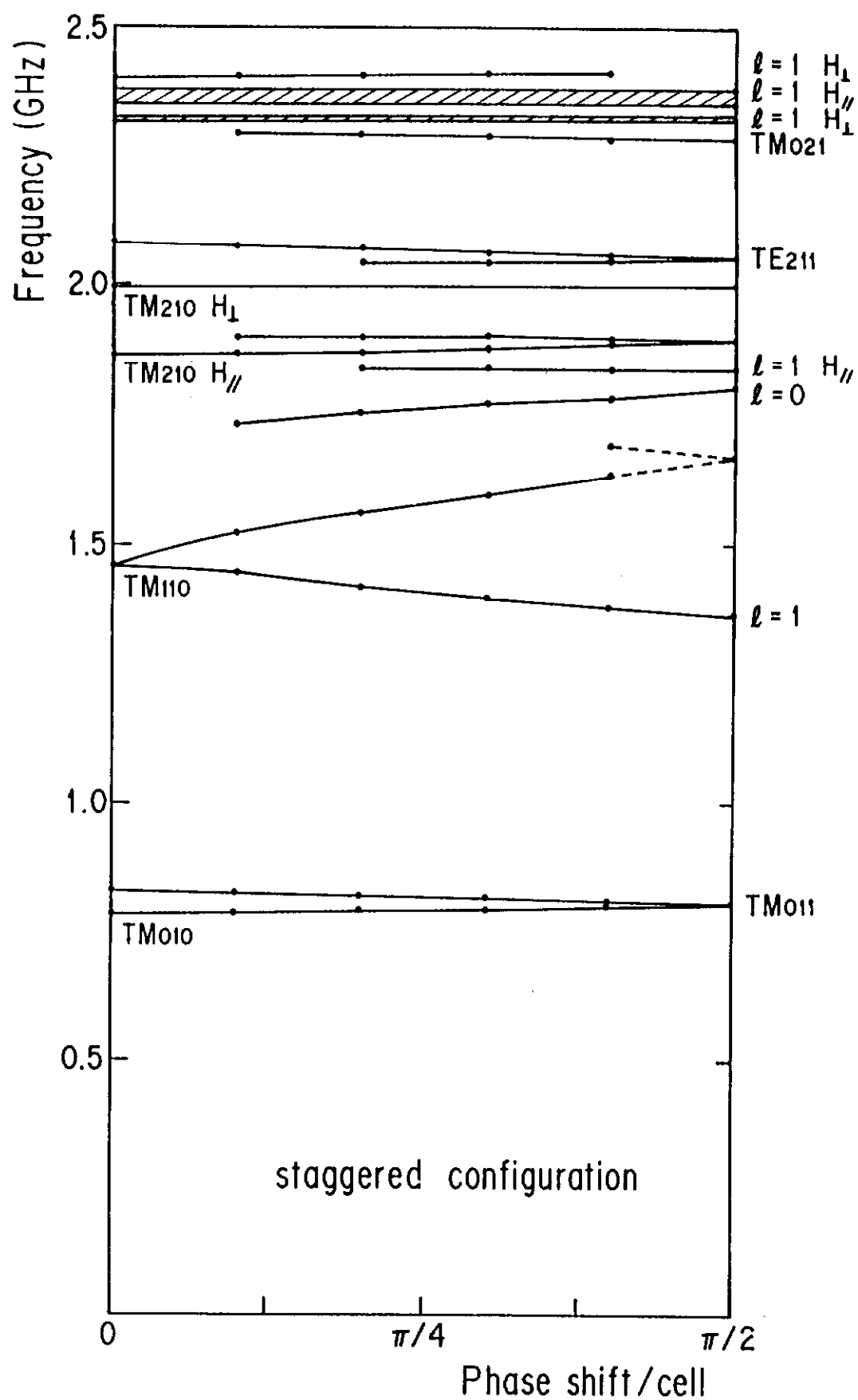configuration of side coupling cells (t-b).

Fig. 8a   Dispersion curve of the staggered configuration.
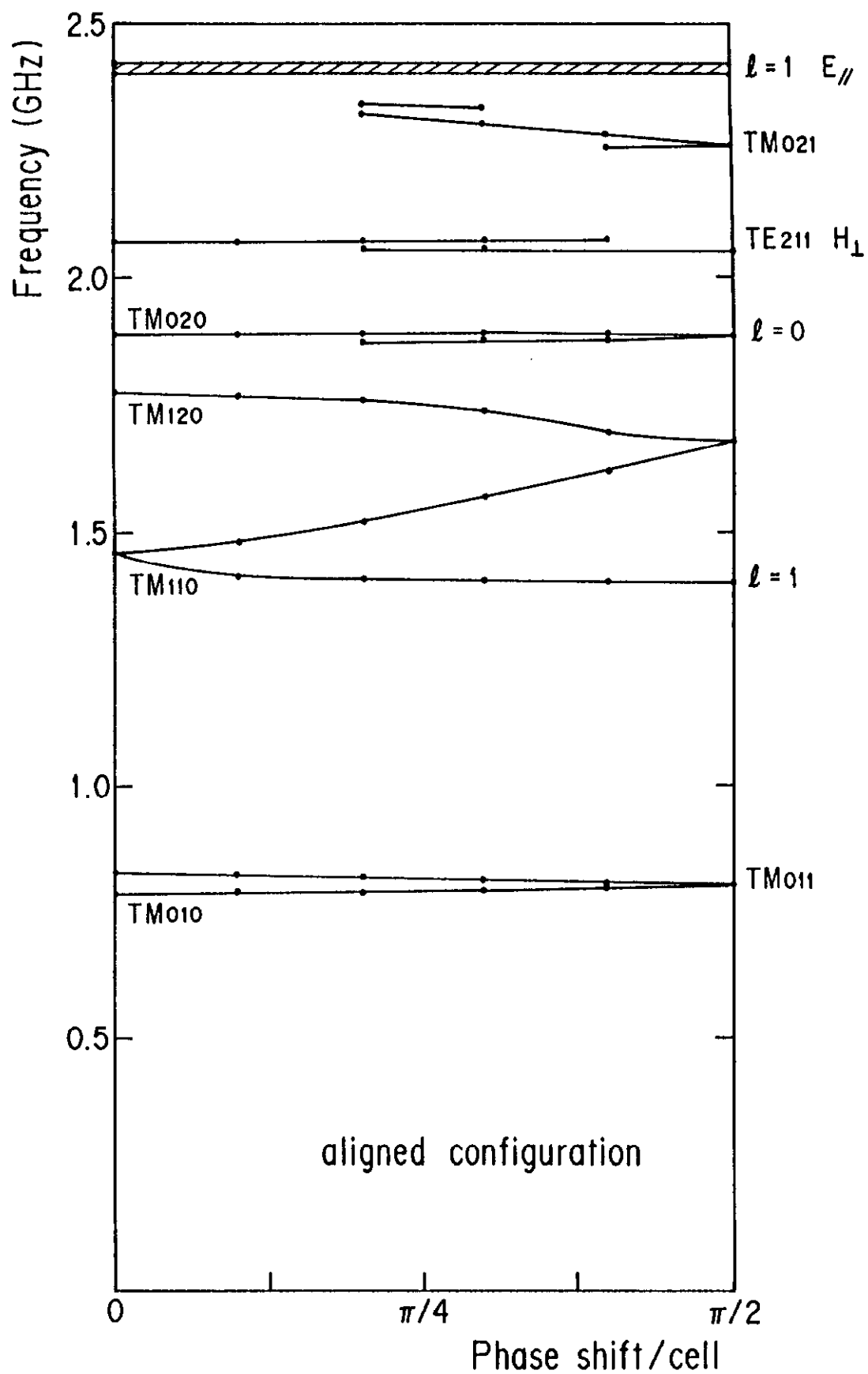
Fig. 8b   Dispersion curve of the aligned configuration.
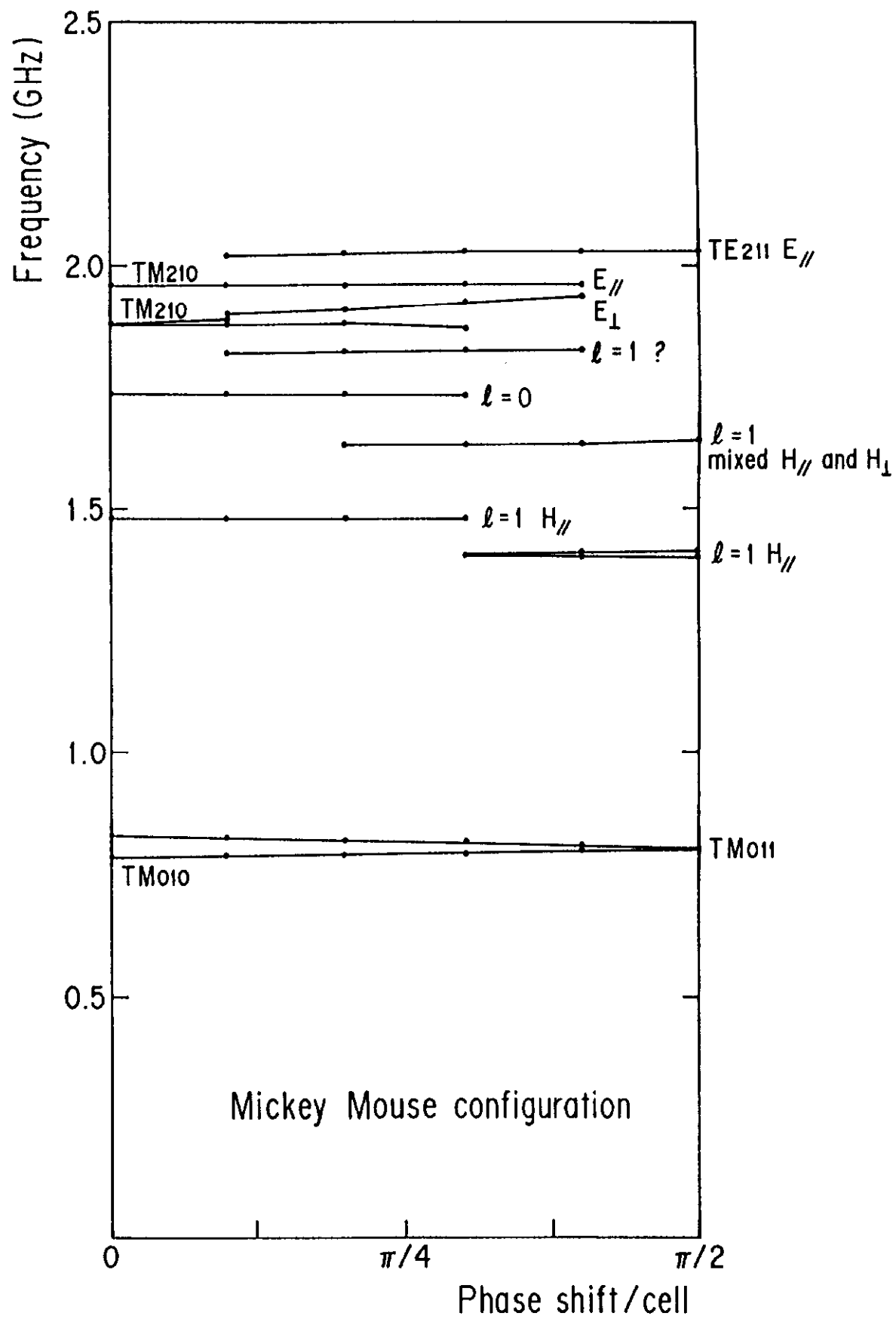
Fig. 8c   Dispersion curve of the Micky Mouse configuration.
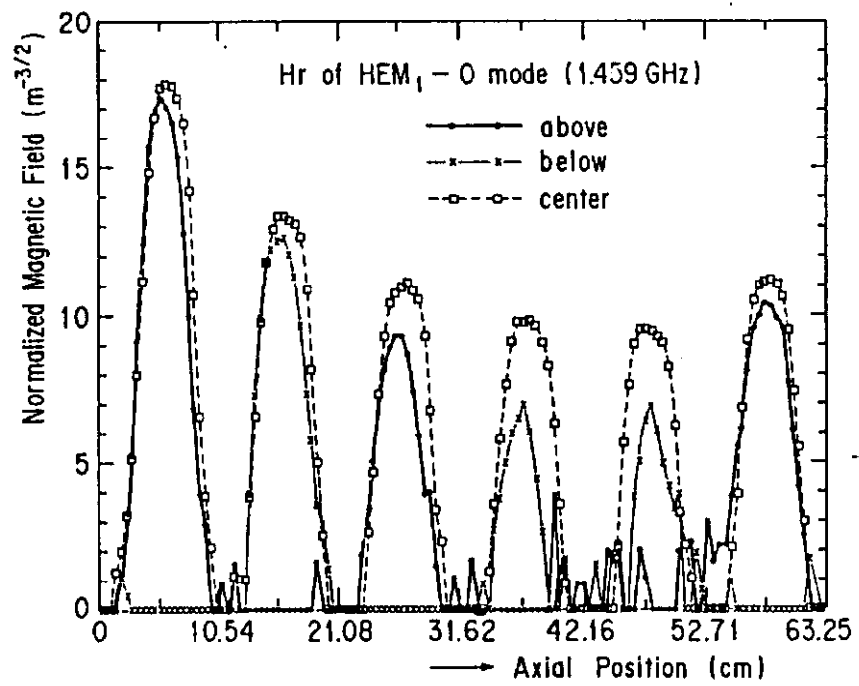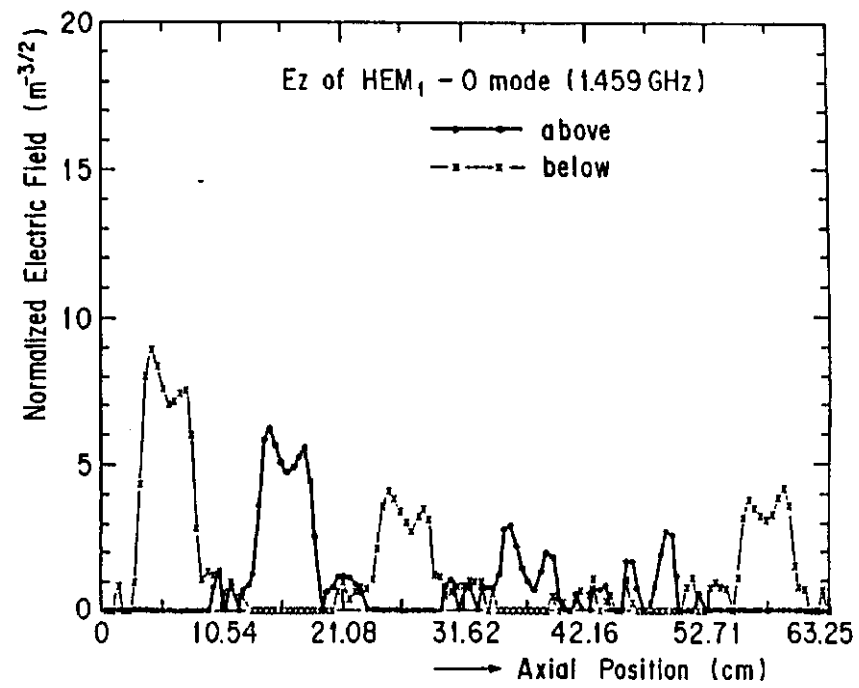
Fig. 9a and b Longitudinal electric and transverse magnetic field of HEM$_1$-0 mode (t-b).
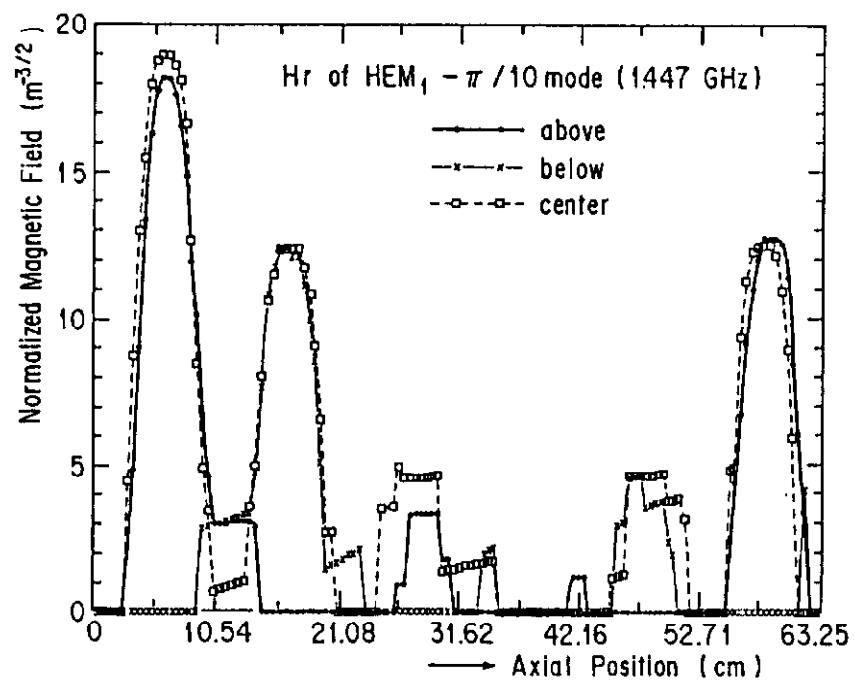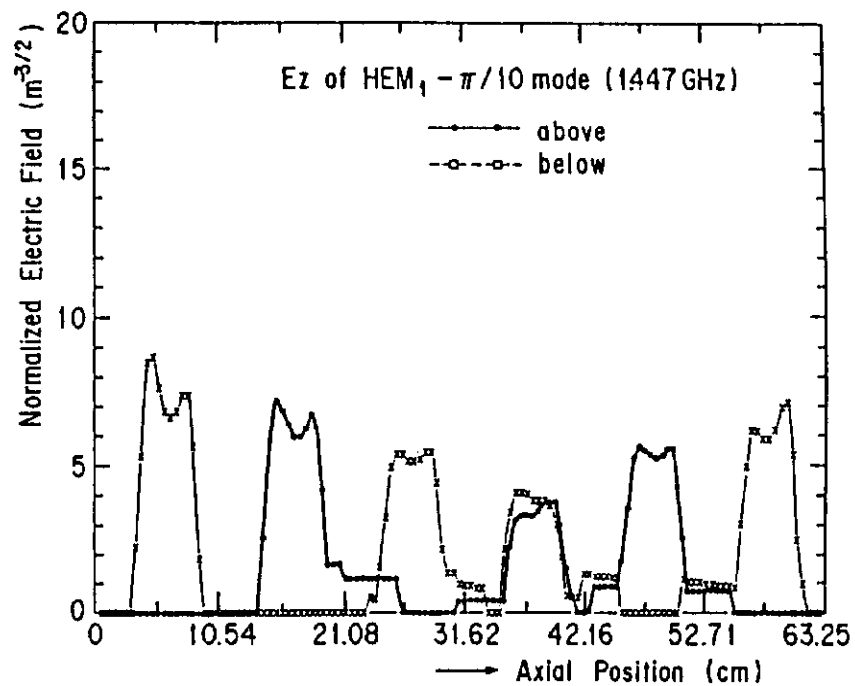
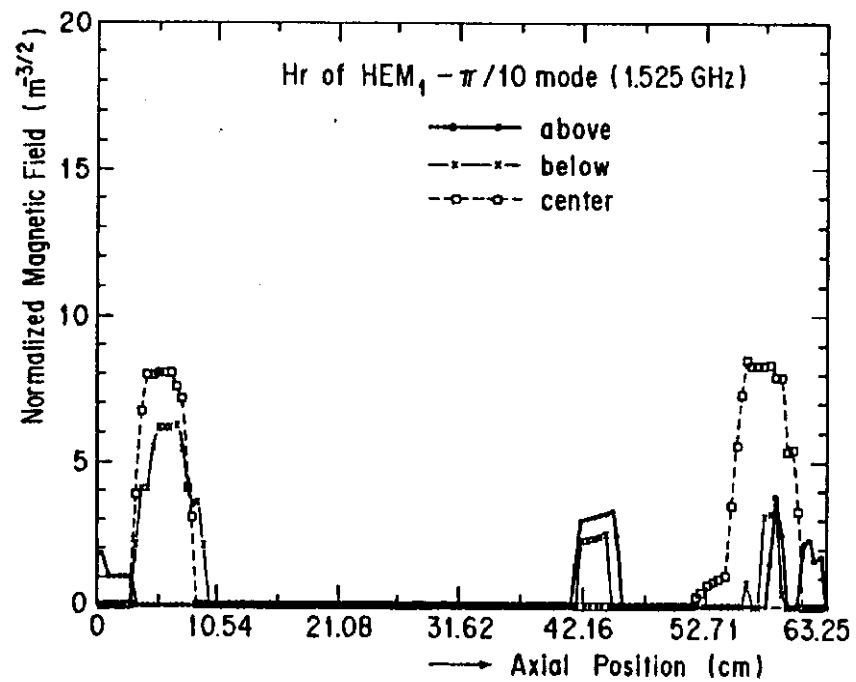Fig. 10a and b   Longitudinal electric and transverse magnetic field
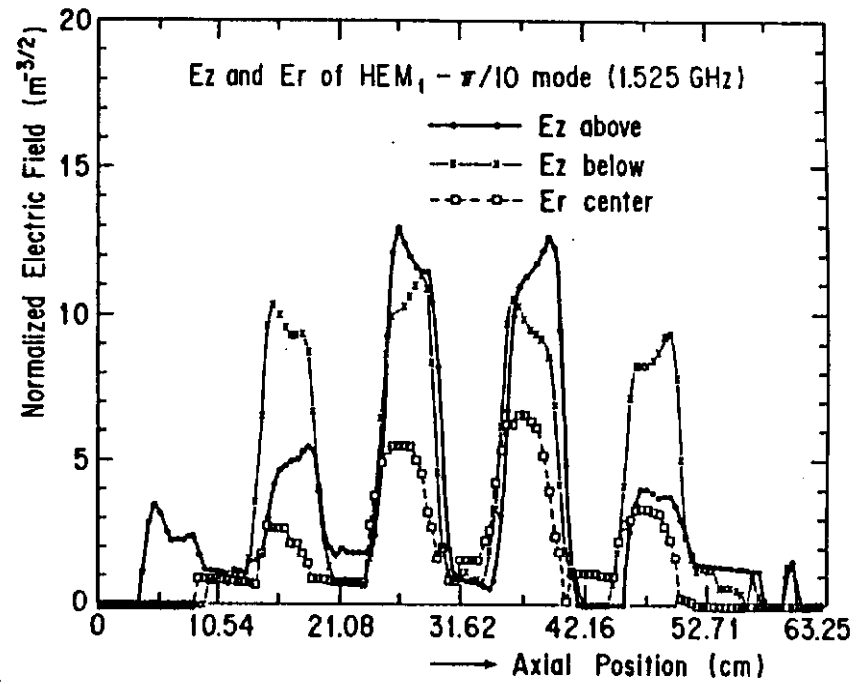of lower HEM_1-$\pi/10$ mode (t-b).

Fig. 11a and b   Electric and transverse magnetic field of higher HEM_1-π/10 mode (t-b).
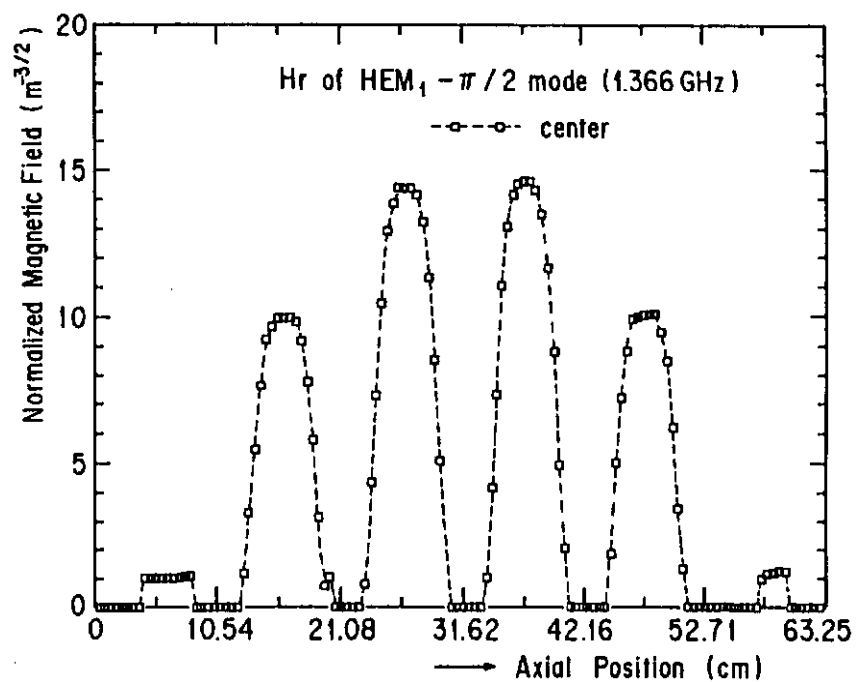
Fig. 12   Transverse magnetic field of lower HEM_1-$\pi/2$ mode.
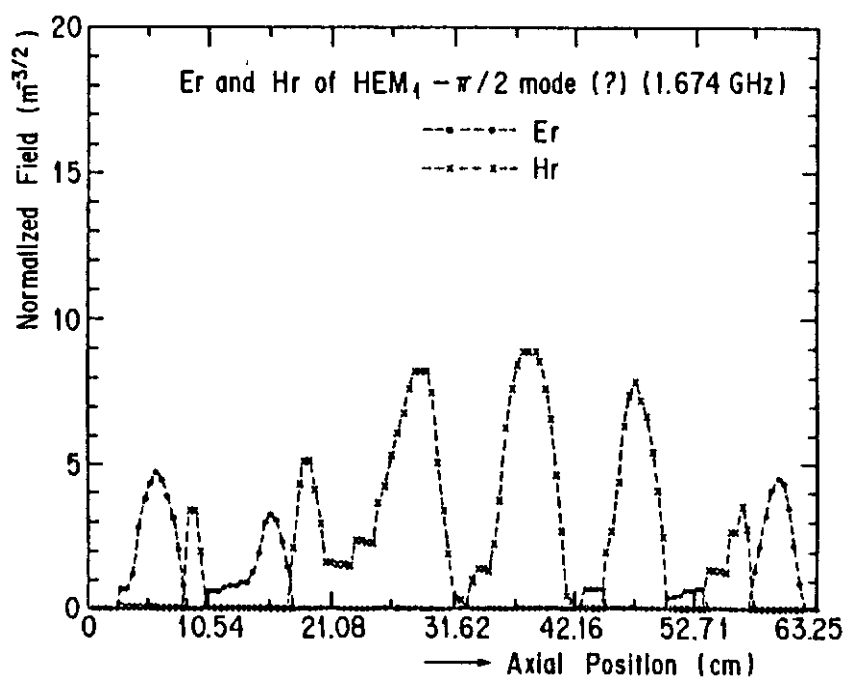

Fig. 13   Transverse magnetic field of higher HEM_1-$\pi/2$ mode.